

000 001 002 003 004 005 006 007 008 009 010 011 012 013 014 015 016 017 018 019 020 021 022 023 024 025 026 027 028 029 030 031 032 033 034 035 036 037 038 039 040 041 042 043 044 045 046 047 048 049 050 051 052 053 CAUSAL PROCESS MODELS: REFRAMING CAUSAL GRAPH DISCOVERY AS A REIN- FORCEMENT LEARNING PROBLEM

Anonymous authors

Paper under double-blind review

ABSTRACT

Most neural models of causality assume static causal graphs, failing to capture the dynamic and sparse nature of physical interactions where causal relationships emerge and dissolve over time. We introduce the Causal Process Framework and its neural implementation, Causal Process Models (CPMs), for learning sparse, time-varying causal graphs from visual observations. Unlike traditional approaches that maintain dense connectivity, our model explicitly constructs causal edges only when objects actively interact, dramatically improving both interpretability and computational efficiency. We achieve this by formulating causal discovery as a multi-agent reinforcement learning problem, where specialized agents sequentially decide which objects are causally connected at each timestep. Our key innovation is a structured representation that factorizes object and force vectors along three learned dimensions (mutability, causal relevance, and control relevance), enabling the automatic discovery of semantically meaningful encodings. We demonstrate that a CPM significantly outperforms dense graph baselines on physical prediction tasks, particularly for longer horizons and varying object counts.

1 INTRODUCTION

Causality plays a fundamental role in building intelligent systems capable of physical reasoning (Gerstenberg et al., 2020). Explicitly modeling causal relationships is increasingly recognized to be crucial for developing robust, generalizable, and interpretable neural network models capable of accurate prediction and effective intervention (Xia et al., 2021). Despite their black-box nature, models such as transformers have demonstrated surprising capacity for causal reasoning (Nichani et al., 2024; Shou et al., 2023; Melnychuk et al., 2022; Dettki et al., 2025). One explanation posits that this is possible due to the attention mechanism forming implicit causal edges between tokens (Vaswani et al., 2017; Rohekar et al., 2023). However, recent work has highlighted a phenomenon known as *over-squashing*, in which the attention mechanism (and related message-passing mechanisms in

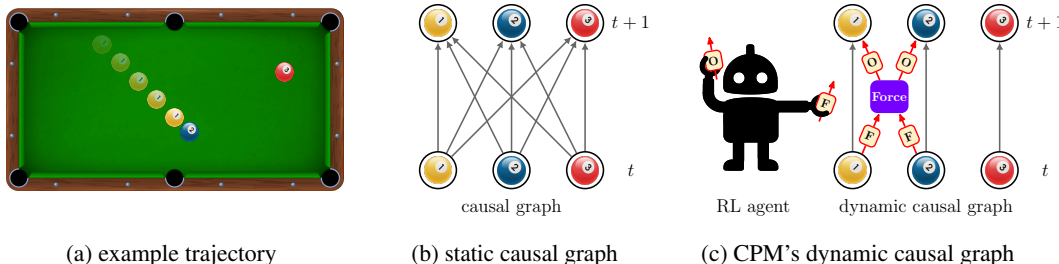


Figure 1: **Dynamic Causality:** (a) In many physical domains, such as a game of billiards, objects interact only sparsely. (b) Static causal graphs must encode *all possible* interactions, resulting in dense connectivity that fails to capture this local sparsity. (c) In a Causal Process Model (CPM), an RL agent dynamically constructs a causal graph by connecting forces and objects through process blocks, yielding a sparse, dynamic causal graph that reflects the actual interactions at each timestep.

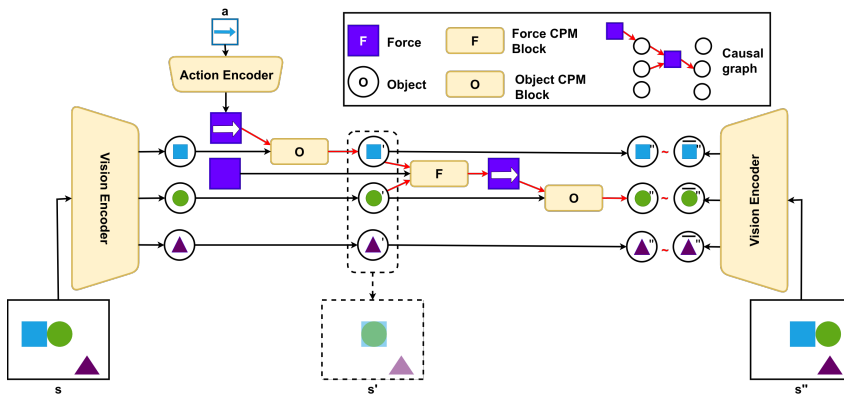


Figure 2: **Model Overview**: Our model has three components: a vision encoder, an action encoder, and a transition function. The transition function is an implementation of a *Causal Process Model*. The state is factorized into distinct object representations, actions are mapped to force representations that act as causal interventions, and the directed edges are causal.

Graph Neural Networks) loses sensitivity to individual tokens or nodes (Barbero et al., 2024a; Alon & Yahav, 2021; Barbero et al., 2024b; Giovanni et al., 2023; 2024; Topping et al., 2022; Scarselli et al., 2009; Battaglia et al., 2018). This compression of information in transformer models can sever causal chains, thus limiting the effectiveness of causal inference.

In contrast, graphical causal models, such as Pearl’s Structural Causal Models (SCMs; Pearl, 2009), explicitly encode causal relationships and thus preserve perfect causal connectivity by design. Yet, a key challenge for SCMs is *causal discovery* (Schölkopf et al., 2021): inferring the causal graph from data. Most existing approaches assume access to a complete dataset and construct a static causal graph, e.g., for all possible interactions of three billiard balls a dense graph is necessary (see Fig. 1a). This assumption is misaligned with the nature of physical environments, where causal influence is typically local in space and sparse in time (Butz, 2017; Pitis et al., 2020; Seitzer et al., 2021; Gumbusch et al., 2021; Lange & Kording, 2025). For instance, objects may only interact upon contact. Recent work has therefore emphasized the importance of *local causal models* (Pitis et al., 2020; Seitzer et al., 2021; Urpí et al., 2024; Lei et al., 2024; Willig et al., 2025) that explain causal connections through the sparsest possible graph, which changes dynamically over time.

Our work aims to bridge these areas by proposing a novel causal framework tailored to capture the dynamics of physical object interactions. We propose **Causal Process Models** (CPMs), as a neural implementation of this framework **casting the construction of sparse dynamic causal graphs as a sequential reinforcement learning (RL) problem**. Instead of relying on dense message passing (e.g., soft attention or standard GNNs, Fig. 1b), CPMs use RL agents to dynamically determine all-or-nothing connections between entities (Fig. 1c). This allows the model to adaptively control connectivity based on the input, avoiding the over-squashing problem and enabling more efficient and interpretable causal reasoning.

Our novel causal framework is designed specifically for modeling the dynamics of physical object interactions, aiming to synthesize the formal rigor of *static dependency* theories, e.g. Pearl’s do-calculus (Pearl, 2009), with the intuitive strengths of *process-based* accounts (Russell, 1948; Salmon, 1984; Skyrms, 1981; Dowe, 2000, see Section 2 below). Our approach explicitly addresses the limitations of Pearlian SCMs by enabling the construction of sparse, time-varying causal graphs that reflect only the active interactions between objects. When modeling two colliding balls for instance, our framework only instantiates a direct causal link between the balls upon contact, for the transfer of momentum, while leaving them causally disconnected otherwise. This yields a computationally efficient model, only scaling with actual rather than all potential interactions, and one that is highly interpretable since the causal graph mirrors intuitive physical processes.

Our main contributions are: 1) We formalize a *Causal Process Framework* (CPF) for local causal modeling in physical environments. 2) We implement this in a neural architecture as a *Causal Process Model* (CPM) to dynamically infer sparse, time-varying causal graphs by framing edge selection as an RL problem. 3) We apply our CPM to physical interaction scenarios, demonstrating superior performance, interpretability, and scalability compared to densely connected models.

108
109

2 RELATED WORK

110
111

2.1 CAUSAL FRAMEWORKS

112
113
Pearl’s (2009) framework of Structural Causal Models (SCMs) is a dominant approach to causal
114
modeling, by representing causal relationships using directed acyclic graphs (DAGs). An SCM can
115
be described as a tuple $\mathcal{C} := (\mathbf{S}, \mathbb{P}(\mathbf{U}))$ where \mathbb{P} is a distribution over the exogenous variables \mathbf{U}
116
(i.e., variables external to the system and not caused by any variable within it) and \mathbf{S} is a collection of
117
structural equations of the form:

118
119
$$V_i = f_{V_i}(\mathbf{Pa}_{V_i}, \mathbf{U}_{V_i}).$$

120

121
122
Each endogenous variable V_i is determined by a function of its parent variables \mathbf{Pa}_{V_i} (i.e., other
123
variables in the system that directly influence V_i) and its associated exogenous noise term \mathbf{U}_{V_i} .124
125
While successful in many domains, standard SCMs require extensions to handle systems characterized
126
by dynamic object interactions; without such extensions, they fail to adequately capture the temporal
127
and structural intricacies of such systems (Rubenstein et al., 2016; Weber, 2016; Blom et al., 2020;
128
Boeken & Mooij, 2024). Consider the simple scenario of two colliding balls shown in Fig. 1a.
129
Representing this within a traditional SCM framework often requires specifying potential causal
130
links between all properties of all objects at all relevant timescales. This leads to densely connected
131
causal graphs (Fig. 1b), with the number of causal edges scaling quadratically with time, even
132
when interactions are sparse in reality. Such dense representations suffer from high computational
133
costs for inference and learning, and crucially, obscure the underlying causal structure, hindering
134
interpretability. Thus, a core challenge is to adapt standard SCMs to dynamically represent only the
135
relevant interactions as they occur, rather than needing to specify all potential dependencies.136
137
Recognizing these limitations, other lines of research offer valuable perspectives, often aligning
138
closely with *causal process theories* (Russell, 1948; Salmon, 1984; Skyrms, 1981; Dowe, 2000).
139
Research in cognitive science, such as Gerstenberg et al. (2020)’s counterfactual simulation models,
140
leverage simulation to assess causality and responsibility in physical events, capturing process-
141
like intuitions. Furthermore, philosophical inquiries into causal processes provide rich conceptual
142
foundations, distinguishing *causal* processes from *pseudo*-processes by focusing on mechanisms
143
like causal lines (Russell, 1948), defining causality in ontological terms (Salmon, 1984), or using
144
conserved quantities (Skyrms, 1981; Dowe, 2000). However, this philosophical tradition lacks the
145
computational formalism required for direct implementation in ML systems. Our Causal Process
146
Framework bridges this gap by providing a computationally tractable formalism that integrates
147
process-based intuitions with graphical causal models, enabling dynamic and sparse representations
148
suitable for learning from visual data in physical environments.149
150

2.2 NEURAL CAUSAL MODELS

151
152
While philosophical causal process theories offer intuitive insights into dynamic physical interactions,
153
their abstract nature limits direct application in scalable machine learning systems. To operationalize
154
these ideas computationally, researchers have sought to integrate causal process intuitions with
155
neural architectures, particularly by embedding SCMs into deep learning frameworks. Previous
156
attempts to reconcile deep learning with SCMs have resulted in Neural Causal Models (NCMs),
157
which model f_{V_i} as feedforward neural nets parametrized by θ_{V_i} (Xia et al., 2021). Yet this solution
158
still suffers from the disadvantage of needing to train arbitrarily many feedforward neural networks
159
for each node across time. To address this parameter explosion, Zecevic et al. (2021) have tried to
160
theoretically quantify the capacity for GNNs to implement SCMs, but are restricted to the assumption
161
of static causal graph. In contrast, Melnychuk et al. (2022) designed a Causal Transformer that
incorporates temporal dynamics to infer causality over time, yet is still unable to yield interpretable
graph representations. This limitation arises from its reliance on the potential outcomes framework
(Rubin, 1978; Robins & Hernan, 2008), which focuses on estimating counterfactual outcomes without
explicitly representing causal relationships as graphs, thus making it less suitable for discovering and
utilizing sparse, time-varying structures.

162 2.3 CAUSAL REINFORCEMENT LEARNING
163

164 Buesing et al. (2019) have tried to take advantage of the Pearlian causality framework by reformulating
165 the MDP graph as an SCM using which they designed a counterfactually-guided policy search. A
166 similar approach has been pursued by Gasse et al. (2023) in which they draw parallels between
167 confounding variables and offline RL. Neither of these approaches factors the MDP state space
168 into distinct object-centric nodes and their causal relations, instead focusing on the aforementioned
169 inherent causality of the MDP structure as suggested by Bareinboim et al. (2021).
170

171 3 CAUSAL PROCESS FRAMEWORK
172

173 Pearl’s structural causal models (SCMs) and do-calculus (Pearl, 2009) provide a powerful foundation
174 for causal reasoning. However, without extensions, it is not straightforward to apply SCM to dynamic
175 physical systems requiring object-centric representations and real-time causal interactions. Prior
176 approaches (Buesing et al., 2019; Gasse et al., 2023) have attempted to bridge model-based RL and
177 causality by representing the full Markov Decision Process (MDP) state s^t using a single node and
178 modeling actions as direct interventions in a static causal graph. However, this approach is limited
179 because it circumvents the problem of inferring the causal structure that generates the underlying
180 environment dynamics (i.e., the causal context; Butz et al., 2025), and focuses only on the causal
181 implications of action sequences.
182

183 3.1 CAUSAL PROCESS MODELS (CPMs)

184 To address the inability of SCMs to capture sparse, time-varying interactions, the computational
185 burden of dense connectivity, and the loss of causal information in over-squashed message-passing,
186 we introduce Causal Process Models (CPMs). CPMs dynamically construct sparse causal graphs that
187 represent only active interactions, enabling both computational efficiency and interpretable causal
188 structure in physical environments.
189

190 We adopt an *object-centric factorization* of states, in which physical objects are represented separately
191 as nodes $\mathcal{O} = \{O_1, O_2, \dots, O_N\}$ (e.g., balls) and interactions between objects are represented as
192 force nodes $\mathcal{F} = \{F_1, F_2, \dots, F_M\}$ (e.g., collisions). At each timestep t , we have object states
193 $\mathcal{O}^t = \{O_1^t, \dots, O_N^t\}$ and force states $\mathcal{F}^t = \{F_1^t, \dots, F_M^t\}$. The key insight is that not all objects
194 interact at all times, hence we need to dynamically determine which causal edges are active.
195

196 3.1.1 DYNAMIC CAUSAL GRAPH CONSTRUCTION

197 To dynamically determine active causal edges in the graph, CPMs employ two types of specialized
198 controller functions: *interaction scope controllers* $\rho_{\mathcal{O}}^t$ determine which objects interact, that is, ex-
199 change forces (e.g., based on spatial proximity), while *effect attribution controllers* $\rho_{\mathcal{O} \leftrightarrow \mathcal{F}}^t$ determine
200 how objects are affected by these interacting forces.
201

202 Formally, each controller outputs probabilistic distributions over possible edge subsets at each
203 timestep. The interaction scope controllers $\rho_{\mathcal{O}}^t$ define a distribution over edge sets $J^t \subseteq \mathcal{O}^t \times \mathcal{F}^t$
204 conditioned on current object states \mathcal{O}^t , yielding $J^t \sim \rho_{\mathcal{O}}^t(\cdot | \mathcal{O}^t)$. Similarly, the effect attribution
205 controllers $\rho_{\mathcal{O} \leftrightarrow \mathcal{F}}^t$ define a distribution over edge sets $I^t \subseteq \mathcal{F}^t \times \mathcal{O}^{t+1}$ conditioned on current object
206 and force states $(\mathcal{O}^t, \mathcal{F}^t)$, yielding $I^t \sim \rho_{\mathcal{O} \leftrightarrow \mathcal{F}}^t(\cdot | \mathcal{O}^t, \mathcal{F}^t)$.
207

208 Within this framework, state evolutions are governed by object and force update functions $f_{\mathcal{O}}$ and $f_{\mathcal{F}}$,
209 which propagate information along the dynamically selected causal edges:
210

$$\begin{aligned} \text{Forces} \quad F_j^t &:= f_{\mathcal{F}} \left(F_j^{t-1}, \left\{ O_i^{t-1} \right\}_{i|(i,j) \in J^{t-1}} \right) & \text{s.t. } J^{t-1} \sim \rho_{\mathcal{O}}^{t-1}, \\ \text{Objects} \quad O_i^t &:= f_{\mathcal{O}} \left(O_i^{t-1}, \left\{ F_j^t \right\}_{j|(j,i) \in I^{t-1}} \right) & \text{s.t. } I^{t-1} \sim \rho_{\mathcal{O} \leftrightarrow \mathcal{F}}^{t-1}. \end{aligned} \quad (1)$$

211 Thus, update functions $f_{\mathcal{F}}$ and $f_{\mathcal{O}}$ are force- and object-specific (respectively) and invariant to the
212 number of inputs (i.e., size of the parent node set). When interventions occur at time step \tilde{t} , they
213 introduce perturbations over object nodes, denoted as $\text{act}(O_*^{\tilde{t}})$ representing externally applied actions
214 (e.g., hitting a billiard ball). Intuitively, this step captures how such external influences propagate
215

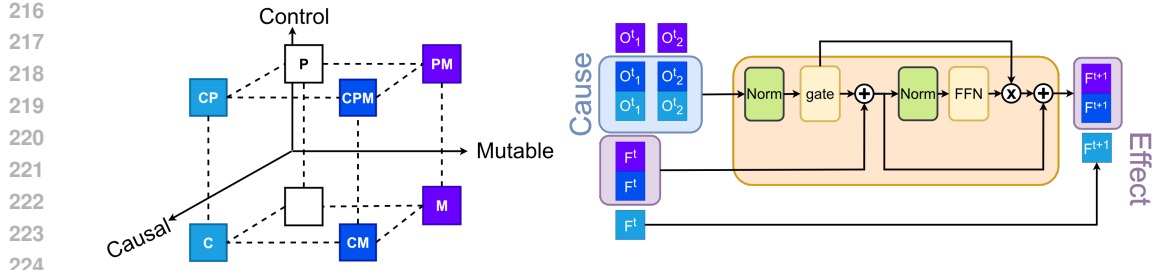


Figure 3: **Causal Process Block** (illustrating f_F): Modified transformer with attention replaced by gate mechanism (see Appendix B.3). Incoming causes O_i^t are pre-selected by the causal controllers. Latent vectors are divided into causal (C), control (P), and mutable (M) regions, enforcing structured updates.

forward in time, akin to resimulating the physical system from the intervention point onward: the model dynamically recomputes the subgraph for all subsequent time steps $t \geq \hat{t}$ by resampling causal edges and updating node states via the controllers and transition functions, ensuring the causal graph reflects the altered dynamics (following Algorithm 1).

3.1.2 CONCRETE EXAMPLE: TWO COLLIDING BALLS

To illustrate, consider a scenario with three balls, where Ball 1 collides with Ball 2 at time t (Fig. 1a). The objects are represented as $\{O_1^t, O_2^t, O_3^t\}$, and a single force node F_1^t mediates the interaction. Here, the interaction scope controller ρ_O^t assigns high probability to the edges $J^t = \{E(O_1^t, F_1^t), E(O_2^t, F_1^t)\}$, indicating that both Ball 1 and Ball 2 contribute to generating the collision force. Similarly, the effect attribution controller $\rho_{O \leftrightarrow F}^t$ assigns high probability to the edges $I^t = \{E(F_1^t, O_1^{t+1}), E(F_1^t, O_2^{t+1})\}$, specifying that the force affects both balls post-collision. The resulting graph is illustrated in Fig. 1c. In contrast, when the balls are far apart and no interaction occurs, both controllers would output empty edge sets, resulting in a sparse graph with only self-connections during that time period (e.g., Ball 3 in Fig. 1c).

3.1.3 INDUCTIVE BIASES

To ground the flexible graph construction in realistic physical principles and mitigate the risk of overfitting to spurious connections, we incorporate two key inductive biases that reflect common patterns in object interactions. **Pairwise Interactions** restrict each force node to connect to exactly two different object nodes. This corresponds to the assumption that typically not more than two objects interact at a certain time step. This restriction can be lifted later to generalize to hypergraphs for more complicated systems (e.g., 3-body problems). **Newton’s Third Law and Force Symmetry** are modeled through our mirroring constraint: when two objects interact, the force node must affect both objects that contributed to it. In physical collisions, forces come in equal and opposite pairs acting on both objects. This design ensures physical consistency while maintaining computational efficiency. In environments with asymmetric interactions (e.g., large objects unaffected by small ones), the learned weights in f_O can effectively set the influence to zero (see Appendix B.1 for formal definitions).

4 MODEL

We base our model implementation on the Contrastively-trained Structured World Model (C-SWM; Kipf et al., 2020). The model consists of an *object-centric vision encoder*, an *action encoder*, and a *transition function* (Fig. 2). We keep the structure of the vision and action encoders intact, but modify the transition function.

The *vision encoder* is a CNN-based object extractor E_{ext} , operating directly on images and outputting I feature maps. Each feature map $m_i^t = [E_{\text{ext}}(s^t)]_i$ acts as an object mask where $[\dots]_i$ is the selection of the i^{th} feature map. An MLP-based object encoder E_{enc} with shared weights across objects maps the flattened feature map m_i^t to object latent representation: $O_i^t = E_{\text{enc}}(m_i^t)$. Additionally, an MLP-based *action encoder* maps action a^t to force latent representation: $F^t = A(a^t)$. Next, we

270 introduce our new transition function (Sec. 4.1) before detailing how to construct the causal graph on
 271 the fly using reinforcement learning (Sec. 4.2).
 272

273 **4.1 CAUSAL PROCESS BLOCK**
 274

275 Our main innovation is the *Causal Process Block* as a neural network implementation of a CPM (Fig.
 276 3). Before introducing the technical details, we need to address a key challenge: not all components
 277 of force and object representations play the same role in causal interactions.
 278

279 **4.1.1 STRUCTURED REPRESENTATIONS**
 280

281 Let us revisit the example of collision between two balls (Fig. 1a). Their masses affect momentum
 282 transfer (causally relevant) but remain unchanged during the collision (immutable). In contrast,
 283 their velocities are both causally relevant and mutable. Meanwhile, visual properties like color may
 284 change due to lighting, but don't affect the collision dynamics (mutable but not causally relevant).
 285 To capture these distinctions and enable our model to learn interpretable encodings that naturally
 286 separate these different physical properties, we factorize our representations along three key binary
 287 subspaces of *Causal Relevance* (C), *Control Relevance* (P), and *Mutability* (M). The binary nature
 288 of each subspace arises from selective routing within the CPM (Fig. 3).
 289

290 Causal Relevance (C) describes whether a component influences the dynamics of other objects.
 291 For instance mass and velocity affect collision outcomes ($C = 1$), but color does not ($C = 0$).
 292 Control Relevance (P) encodes whether a component is used by the control/policy functions for
 293 decision-making. For example, a controller deciding which balls are about to collide will rely on
 294 current positions and velocities ($P = 1$), but will ignore other properties such as mass or purely visual
 295 features like color ($P = 0$). Mutability (M) captures whether a component can change over time
 296 through interactions. For instance, an object being struck may change velocity ($M = 1$), while its
 297 mass remains constant ($M = 0$). Importantly, while the factorization structure is fixed (based on C ,
 298 P , and M), the model *learns* which specific features belong to each category through training. This
 299 hard architectural partitioning forces the model to discover semantically meaningful, disentangled
 300 representations that align with intuitive physical concepts.
 301

302 **4.1.2 TECHNICAL IMPLEMENTATION**
 303

304 We use two feedforward neural networks, $f_F(\dots; \theta_F)$ and $f_O(\dots; \theta_O)$, shared by all the force and
 305 object nodes respectively. The force vector $F_j^t := \bigoplus_{C,P,M \in \{1,0\}, (C,P,M) \neq (0,0,0)} F_j^{t,CPM}$ is the
 306 concatenation of all combinations of the C , P , M dimensions except for $(C, P, M) = (0, 0, 0)$,
 307 which must be omitted since forces, by definition, do not contain subspaces that are irrelevant to the
 308 causal process. This results in $2^3 - 1 = 7$ sub-vectors of equal size d_F , where a sub-vector's identity
 309 determines how it is processed by the neural networks: The object-update function f_O and force-
 310 update function f_F operate exclusively on the causally relevant subspace ($C = 1$), while mutable
 311 parts are updated and immutable parts are copied unchanged ($M = 0$; Fig. 3). The object vector
 312 O_i^t is more straightforwardly divided into $2^3 = 8$ subvectors, i.e., all possible combinations of the
 313 C , P , M dimensions, including the $(C, P, M) = (0, 0, 0)$ subspace: $O_i^t := \bigoplus_{C,P,M \in \{1,0\}} O_i^{t,CPM}$.
 314 The extra subspace is present here for the network to learn to shift visual input features that are
 315 irrelevant to the causal process into this subspace, for example the object's color in a collision
 316 event (See Appendices B.2 and B.3 for details). Note that the implementation of the causal process
 317 blocks $f_O(\dots | \theta_O)$ and $f_F(\dots | \theta_F)$ is similar to that of transformer blocks, but with the attention
 318 mechanism (Vaswani et al., 2017) replaced by indices of the chosen force and object nodes (tokens in
 319 transformers; see Appendix B.3 and Fig. 3 for more details). Unlike the attention mechanism of the
 320 transformer, I^t , J^t can also be an empty set. This is analogous to transformer attention assigning
 321 zero weight to all the tokens, which they cannot do by design.
 322

323 **4.2 CAUSAL CONTROLLER**

324 The main proposal of our model is that we perform graph construction through sequential decision
 325 making using the interaction scope and effect attribution controllers. We treat causal discovery as a
 326 multi-agent RL problem. One agent (the interaction scope policy $\pi_O(\mathcal{O}^t) := \rho_O^t$) determines the
 327

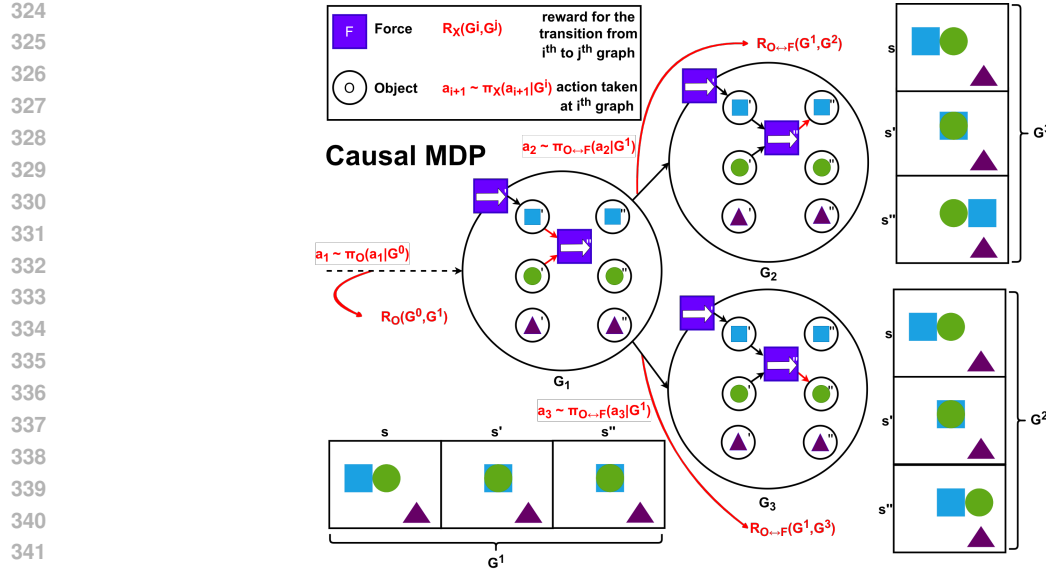


Figure 4: **Causal MDP** used by the reactive agents to construct causal process graphs. Agents successively add edges to the causal graph. Each causal graph hypothesis corresponds to a potential sequence of frames.

scope of interacting objects, and another (the effect attribution policy $\pi_{O \leftrightarrow F}(\mathcal{O}^t, \mathcal{F}^{t+1}) := \rho_{O \leftrightarrow F}^t$) determines how force effects are attributed .

More specifically, the chosen indices I^t and J^t are provided by the agents $\pi_{O \leftrightarrow F}$ and π_O . The two agents alternate outputting an action. An action taken by π_O corresponds to two edge additions $E(O_i^t, F^{t+1}), E(O_j^t, F^{t+1}), i \neq j$ to the graph (selecting a pair of objects for interaction). Whereas an action taken by $\pi_{O \leftrightarrow F}$ results in either one or two edge additions $E(F^t, O_i^t), E(F^t, O_j^t)$ (attributing the force effect to either one or both objects; see Fig. 4). The index set I^t is sampled using the policy of the agent $\pi_{O \leftrightarrow F}$. Note that the policies only utilize the Control Relevant (P) features of the latent representations:

$$I^t \sim \pi_{O \leftrightarrow F}(I^t | G^t, W_O, W_F) = \text{softmax}\left(Q_{O \leftrightarrow F}(G^t, I^t | W_O, W_F)\right) \\ = \text{softmax}\left(\frac{(F^{t, C1M} W_F) \left([O_i^{t, C1M}; O_j^{t, C1M}; (O_i^{t, C1M} + O_j^{t, C1M}) / 2] W_O \right)^T}{d}\right), \quad (2)$$

where $W_O \in \mathbb{R}^{4d_O \times d}$, $W_F \in \mathbb{R}^{4d_F \times d}$, and $Q_{O \leftrightarrow F}$ is the corresponding Q-value. J^t , on the other hand, is sampled using the policy of the agent π_O :

$$J^t \sim \pi_O(J^t | G^t, W_{\tilde{O}}) = \sigma(Q_O(G^t, J^t | G^t, W_{\tilde{O}})) = \sigma((O_i^{t, C1M} W_{\tilde{O}}) \cdot (O_j^{t, C1M} W_{\tilde{O}})), \quad (3)$$

where $W_{\tilde{O}} \in \mathbb{R}^{4d_O \times d}$, σ is the sigmoid function, and Q_O is the corresponding Q-value.

We then define separate reward functions for $\pi_{O \leftrightarrow F}$ and π_O , modeled by MLPs parameterized by $\theta_{R_{O \leftrightarrow F}}$ and θ_{R_O} respectively:

$$R_{O \leftrightarrow F}(G^t, G^{t+1} | \theta_{R_{O \leftrightarrow F}}) = \text{MLP}\left(G_V^t, \mathbb{1}_{E(F^t, O_i^t)}, \mathbb{1}_{E(F^t, O_j^t)}, G_V^{t+1} | \theta_{R_{O \leftrightarrow F}}\right), \\ R_O(G^t, G^{t+1} | \theta_{R_O}) = \text{MLP}\left(G_V^t, \mathbb{1}_{E(O_i^t, F^{t+1}) \wedge E(O_j^t, F^{t+1})}, G_V^{t+1} | \theta_{R_O}\right), \quad (4)$$

where $G^t := (G_V^t, G_E^t)$ is the graph at time t and $\mathbb{1}_{E(\cdot, \cdot)}$ indicates the presence or absence of the edge $E(\cdot, \cdot)$. These reward functions are learned through inverse reinforcement learning (IRL), where the goal is to find a reward function whose corresponding optimal policy would select causal edges that would minimize prediction error.

378

5 TRAINING

380

5.1 TRAINING OVERVIEW AND REWARD LEARNING

382 Our training procedure addresses a fundamental challenge: jointly learning the causal dynamics
 383 model and the policy for selecting causal edges. The key insight is that good edge selections lead to
 384 better prediction accuracy, which we use as an implicit reward signal through inverse reinforcement
 385 learning (Ng & Russell, 2000).

386 The optimization has three objectives: 1) The CPM should accurately predict future states given the
 387 selected causal edges; 2) the RL agents should select edges that minimize prediction error; 3) the
 388 reward functions R_O and $R_{O \leftrightarrow F}$ should capture which edge selections lead to better predictions.
 389 At convergence, the agents select sparse causal graphs that capture only the active interactions,
 390 leading to both computational efficiency and interpretability. The optimum of the combined CPM
 391 and RL objectives is reached when the agents consistently construct causal graphs that minimize the
 392 prediction error; at this point the learned reward networks stabilize.

393

5.2 TRAINING PROCEDURE

395 The overall goal is to learn a predictive world model (CPM) whose structure is determined by
 396 the policies $(\pi_O, \pi_{O \leftrightarrow F})$. This requires optimizing both the model parameters Θ and the policy
 397 parameters $\Psi := [W_O, W_F, W_{\tilde{O}}]$. We achieve this using a 3-stage procedure that also involves
 398 expectation-maximization (EM) with alternating optimization (Dempster et al., 1977).

400 **1. Prediction.** At this stage, we freeze all the weights except $\Theta = [\theta_V; \theta_A; \theta_O; \theta_F]$ and sample edges
 401 $\{I^\tau, J^\tau\}_\tau$ using frozen controllers. This allows the vision encoder, action encoder, and transition
 402 functions (f_O, f_F) to learn useful representations before the controllers get the chance to optimize
 403 their behavior on these representations. We train the model parameters Θ using contrastive loss (Kipf
 404 et al., 2020):

$$\mathcal{L}_{\text{pred}}(\Theta | \beta, \mathcal{D}_{\text{pred}}) = \left\| \text{CPM} \left(V(s^t | \theta_V), A(a^t | \theta_A), (I^\tau, J^\tau)_{t_\tau} | \theta_O, \theta_F \right) - V(s^{t+1} | \theta_V) \right\| + \max(0, \beta - \|V(\tilde{s}^t | \theta_V) - V(s^{t+1} | \theta_V)\|) \quad (5)$$

409 where $\mathcal{D}_{\text{pred}} = \{(s^t, a^t, s^{t+1}), \tilde{s}^t, \{(G^{t_\tau}, I^{t_\tau}, J^{t_\tau}, G^{t_{\tau+1}})\}_\tau\}_t$, V and A are the vision and action
 410 encoders, \tilde{s}^t is a negative example sampled from the experience buffer, and the hinge margin β is set
 411 to 1 (following Kipf et al., 2020).

412 **2. Expectation.** In the second stage, we freeze all the weights but $\Theta_R = [\theta_{R_{O \leftrightarrow F}}; \theta_{R_O}]$ and use
 413 temporal difference (TD) loss (Watkins & Dayan, 1992) to learn reward functions:

$$\mathcal{L}_{\text{TD}}(\Theta_R | \mathcal{D}_{\text{TD}}, \Psi) = \sum_{X \in \{\mathcal{O} \leftrightarrow \mathcal{F}, \mathcal{O}\}} \sum_{\tau} \left\| \underbrace{R_X(G^\tau, G^{\tau+1} | \theta_{R_X})}_{\text{learned}} - \underbrace{\left(Q_X(G^\tau, I_X^\tau | \Psi) - \gamma \max_{I_X^{\tau+1}} Q_X(G^{\tau+1}, I_X^{\tau+1} | \Psi) \right)}_{\text{target}} \right\| \quad (6)$$

420 where $\mathcal{D}_{\text{TD}} = \{(G^\tau, I_O^\tau, I_{O \leftrightarrow F}^\tau, G^{\tau+1})\}_\tau$ and we set $\gamma = 0.9$.

421 **3. Maximization.** During the third stage, we freeze all but the policy parameters Ψ and use the same
 422 TD loss from above with target and learned terms reversed. The agents learn to select edges based on
 423 the rewards $R_{O \leftrightarrow F}$ and R_O .

424 The overall optimization landscape is complex; the optimum represents a state where the agents select
 425 the sparse causal graph that yields the minimal prediction loss for the CPM, and simultaneously, the
 426 reward MLPs stabilize under the IRL objective.

428

6 EXPERIMENTS

431 We hypothesize that our model outperforms models that assume dense causal graphs to capture
 432 physical interactions in: 1) longer prediction horizons; 2) test-time generalization across unobservable

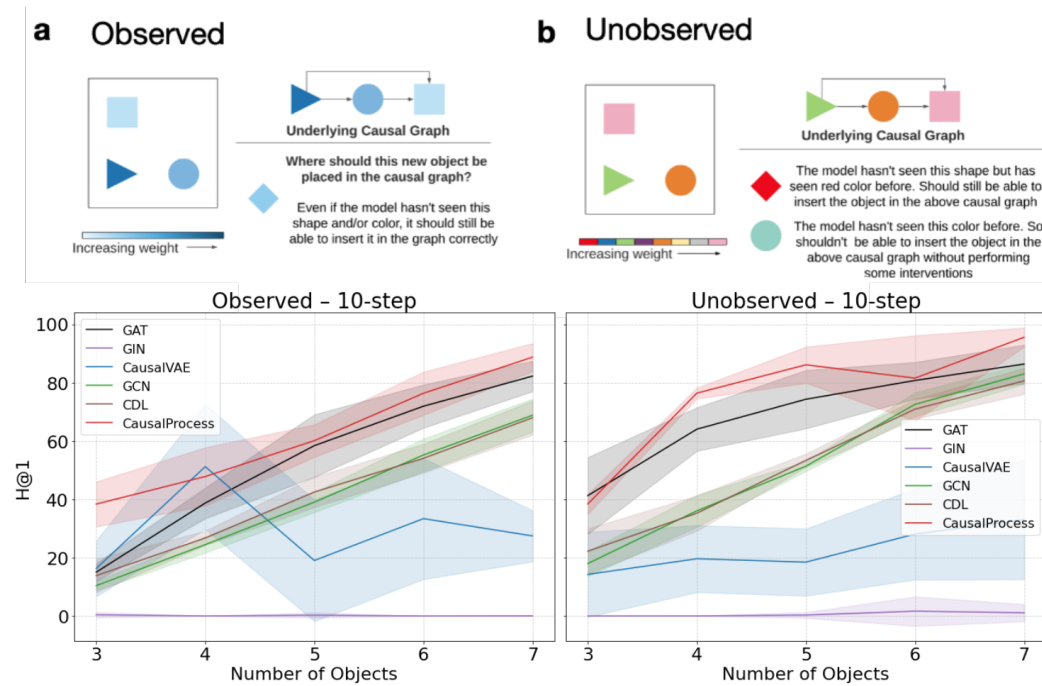


Figure 5: **Prediction results for a synthetic physics environment** in a) observed and b) unobserved settings (Ke et al., 2021). **Top:** Description of the task. **Bottom:** Prediction metric vs number of objects after 10 steps (average of 10 seeds).

properties; 3) robustness with regards to the number of objects in the scene; 4) solving downstream tasks. We use the *physics environment* designed by Ke et al. (2021) to empirically answer these questions (Fig. 5 top). The environment consists of different objects colored according to their weights. The only force in this environment is pushing (double-pushes are not allowed) and only heavier objects can push lighter ones. The environment has two settings: an *observed* setting (Fig. 5a) where weight corresponds to the intensity of a particular color and an *unobserved* setting (Fig. 5b) where different colors did not systematically map to different weights.

6.1 COMPARISON BASELINES

We compare our model against 10 baselines, a graph attention network (GAT) (Veličković et al., 2018), a graph isomorphism network (GIN) (Xu et al., 2019), a causal variational auto-encoder (CausalVAE) (Yang et al., 2021), a graph convolutional network (GCN) (Kipf & Welling, 2017), a causal dynamics learning network (CDL) (Wang et al., 2022), a graph neural network (GNN) (Scarselli et al., 2009), a transformer network (Vaswani et al., 2017), a recurrent independent mechanisms (RIM) network (Goyal et al., 2021b), a schema / object-file factorization network (SCOFF) (Goyal et al., 2021a), and a modular network which has a separate MLP to model each object's dynamics (Ke et al., 2021).

6.2 PREDICTION METRICS

To investigate robustness towards the length of prediction horizons, we trained the model to make 1-step predictions in the *Observed* setting with 5 objects and then tested for 5 (Fig. 9) and 10 steps (Fig. 5a bottom, Fig. 7). We used Hits at Rank 1 (H@1) to measure model performance as an all-or-nothing metric measuring how often the rank of the predicted representation was 1 when ranked against all reference state representations. Here, our model broadly outperformed the baseline models, with the gap increasing over longer time horizons.

Next, to estimate the test-time generalization across unobservable properties, we trained our model in the *Unobserved* setting where generalization at test time is harder due to previously unseen weights.

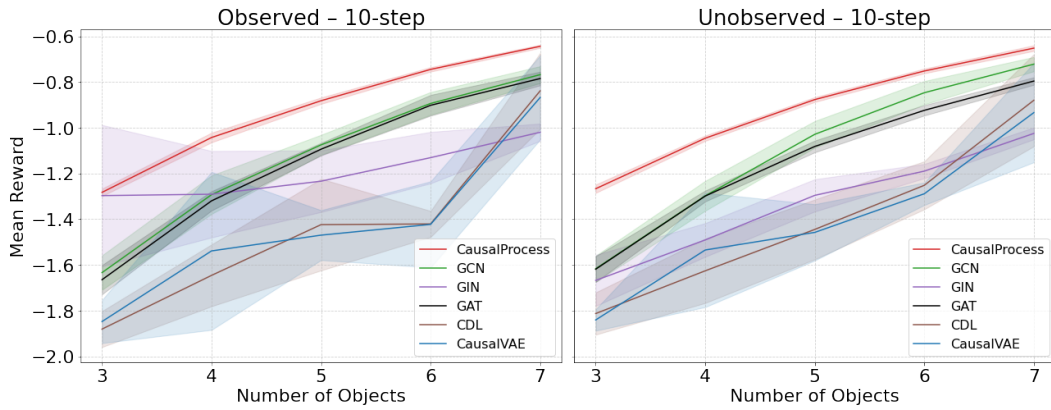


Figure 6: **Downstream RL results** over number of objects. Mean reward vs number of objects. All results are the average of 10 seeds

Again, our model broadly outperformed the baselines displaying capacity to generalize also in this domain (Fig. 5b bottom; see Fig. 7 and Fig. 9 for more results).

6.3 DOWNSTREAM RL TASKS

To make sure the above metrics overlap with the learned model’s usefulness for downstream tasks, we also tested our CPM’s capacity to serve as a world model for a model-based RL agent. The agent’s task was to move an object to a certain location each taken step resulting in negative reward. In both Observed and Unobserved settings, the agent with CPM as model of the environment broadly outperformed the baselines for all objects in 10-step unrolling of the learned model (Fig. 6, Fig. 8).

7 DISCUSSION

In this paper, we introduced the Causal Process Framework (CPF) as a novel approach for modeling the dynamics of physical object interactions. Our key contribution is the Causal Process Model (CPM), which implements this framework by treating the edge distributions inherent to CPF as a reinforcement learning policy. Instead of the soft, dense connections typical of many baselines (Veličković et al., 2018; Goyal et al., 2021a; Xu et al., 2019; Yang et al., 2021; Kipf & Welling, 2017; Wang et al., 2022; Scarselli et al., 2009; Vaswani et al., 2017; Goyal et al., 2021b), our model employs RL agents to dynamically construct sparse, time-varying causal graphs. Our experiments in a simulated physics environment (Ke et al., 2021) show that this approach not only improves prediction accuracy and downstream task performance compared to baselines, but also excels in generalization and scalability.

The superior performance of our model, particularly over longer prediction horizons and with a varying number of objects, lends strong support to our central hypothesis. We argue that by explicitly modeling only active causal links, the CPM avoids the pitfalls of dense message-passing architectures (Barbero et al., 2024a; Alon & Yahav, 2021; Barbero et al., 2024b; Giovanni et al., 2023; 2024; Topping et al., 2022; Scarselli et al., 2009; Battaglia et al., 2018). Our discrete, “all-or-nothing” connections, determined by a goal-oriented RL agent, preserve the salience of individual interactions. This leads to more robust and precise world models, which proved crucial for the model-based RL agent’s success in downstream tasks. Furthermore, the model’s ability to generalize to unobserved object properties suggests that it learns an underlying model of physical dynamics rather than memorizing superficial correlations.

Despite these promising results, the present work has several limitations that open clear avenues for future research. A crucial next step is to deepen the analysis of the learned representations. To do so, the semantic content of the force and object sub-vectors could be decoded to verify that our inductive biases are indeed effective in fostering an interpretable internal structure. To provide further validation our claims of causal discovery, we will be necessary to compare the inferred graphs against the ground-truth interaction graphs of the simulation, providing a quantitative measure of the model’s ability to recover the true causal processes.

540 REFERENCES
541

542 Uri Alon and Eran Yahav. On the bottleneck of graph neural networks and its practical implications.
543 In *9th International Conference on Learning Representations, ICLR 2021, Virtual Event, Austria,*
544 *May 3-7, 2021*. OpenReview.net, 2021. URL <https://openreview.net/forum?id=i80OPhOCVH2>.

545 Federico Barbero, Andrea Banino, Steven Kapturowski, Dharshan Kumaran, João G. M. Araújo, Alex
546 Vitvitskyi, Razvan Pascanu, and Petar Velickovic. Transformers need glasses! information over-
547 squashing in language tasks. *CoRR*, abs/2406.04267, 2024a. doi: 10.48550/ARXIV.2406.04267.
548 URL <https://doi.org/10.48550/arXiv.2406.04267>.

549 Federico Barbero, Ameya Velingker, Amin Saberi, Michael M. Bronstein, and Francesco Di Giovanni.
550 Locality-aware graph rewiring in gnns. In *The Twelfth International Conference on Learning*
551 *Representations, ICLR 2024, Vienna, Austria, May 7-11, 2024*. OpenReview.net, 2024b. URL
552 <https://openreview.net/forum?id=4Ua4hKiAJX>.

553 Elias Bareinboim, S Lee, and J Zhang. An introduction to causal reinforcement learning, 2021.

554 Peter W. Battaglia, Jessica B. Hamrick, Victor Bapst, Alvaro Sanchez-Gonzalez, Vinícius Flores
555 Zambaldi, Mateusz Malinowski, Andrea Tacchetti, David Raposo, Adam Santoro, Ryan Faulkner,
556 Çağlar Güçehre, H. Francis Song, Andrew J. Ballard, Justin Gilmer, George E. Dahl, Ashish
557 Vaswani, Kelsey R. Allen, Charles Nash, Victoria Langston, Chris Dyer, Nicolas Heess, Daan
558 Wierstra, Pushmeet Kohli, Matthew M. Botvinick, Oriol Vinyals, Yujia Li, and Razvan Pascanu.
559 Relational inductive biases, deep learning, and graph networks. *CoRR*, abs/1806.01261, 2018.
560 URL <http://arxiv.org/abs/1806.01261>.

561 Tineke Blom, Stephan Bongers, and Joris M. Mooij. Beyond structural causal models: Causal con-
562 straints models. In Ryan P. Adams and Vibhav Gogate (eds.), *Proceedings of The 35th Uncertainty*
563 *in Artificial Intelligence Conference*, volume 115 of *Proceedings of Machine Learning Research*,
564 pp. 585–594. PMLR, 22–25 Jul 2020. URL <https://proceedings.mlr.press/v115/blom20a.html>.

565 Philip A. Boeken and Joris M. Mooij. Dynamic structural causal models. 2024. URL <https://api.semanticscholar.org/CorpusID:270213849>.

566 Lars Buesing, Theophane Weber, Yori Zwols, Nicolas Heess, Sébastien Racanière, Arthur Guez,
567 and Jean-Baptiste Lespiau. Woulda, coulda, shoulda: Counterfactually-guided policy search.
568 In *7th International Conference on Learning Representations, ICLR 2019, New Orleans, LA,*
569 *USA, May 6-9, 2019*. OpenReview.net, 2019. URL <https://openreview.net/forum?id=BJG0voC9YQ>.

570 Martin V. Butz. Which structures are out there? learning predictive compositional concepts based on
571 social sensorimotor explorations, 2017. ISSN 978-3-95857-138-9.

572 Martin V. Butz, Maximilian Mittenbühler, Sarah Schwöbel, Asya Achimova, Christian Gumbisch,
573 Sebastian Otte, and Stefan Kiebel. Contextualizing predictive minds. *Neuroscience & Biobehavioral Reviews*, 168:105948, 2025. ISSN 0149-7634. doi: <https://doi.org/10.1016/j.neubiorev.2024.105948>. URL <https://www.sciencedirect.com/science/article/pii/S0149763424004172>.

574 Arthur P. Dempster, Nan M. Laird, and Donald B. Rubin. Maximum likelihood from incomplete
575 data via the EM algorithm. *Journal of the Royal Statistical Society. Series B (Methodological)*, 39
576 (1):1–38, 1977. doi: 10.1111/j.2517-6161.1977.tb01600.x. URL <http://www.jstor.org/stable/2984875>. JSTOR: 2984875.

577 Hanna M Dettki, Brenden M Lake, Charley M Wu, and Bob Rehder. Do large language models
578 reason causally like us? even better? *arXiv preprint arXiv:2502.10215*, 2025.

579 Phil Dowe. *Physical Causation*. New York, 2000.

580 Maxime Gasse, Damien Grasset, Guillaume Gaudron, and Pierre-Yves Oudeyer. Using confounded
581 data in latent model-based reinforcement learning. *Trans. Mach. Learn. Res.*, 2023, 2023. URL
582 <https://openreview.net/forum?id=nFWRuJXPkU>.

594 Tobias Gerstenberg, Noah D. Goodman, David A. Lagnado, and Joshua B. Tenenbaum. A counterfac-
 595 tual simulation model of causal judgments for physical events. *Psychological review*, 2020. URL
 596 <https://api.semanticscholar.org/CorpusID:235361720>.

597

598 Francesco Di Giovanni, Lorenzo Giusti, Federico Barbero, Giulia Luise, Pietro Lio, and Michael M.
 599 Bronstein. On over-squashing in message passing neural networks: The impact of width, depth,
 600 and topology. In Andreas Krause, Emma Brunskill, Kyunghyun Cho, Barbara Engelhardt, Sivan
 601 Sabato, and Jonathan Scarlett (eds.), *International Conference on Machine Learning, ICML 2023,*
 602 *23-29 July 2023, Honolulu, Hawaii, USA*, volume 202 of *Proceedings of Machine Learning Re-
 603 search*, pp. 7865–7885. PMLR, 2023. URL <https://proceedings.mlr.press/v202/di-giovanni23a.html>.

604

605 Francesco Di Giovanni, T. Konstantin Rusch, Michael M. Bronstein, Andreea Deac, Marc Lackenby,
 606 Siddhartha Mishra, and Petar Velickovic. How does over-squashing affect the power of gnns?
 607 *Trans. Mach. Learn. Res.*, 2024, 2024. URL <https://openreview.net/forum?id=KJRQvRWNs>.

608

609 Anirudh Goyal, Alex Lamb, Phanideep Gampa, Philippe Beaudoin, Charles Blundell, Sergey Levine,
 610 Yoshua Bengio, and Michael Curtis Mozer. Factorizing declarative and procedural knowledge in
 611 structured, dynamical environments. In *International Conference on Learning Representations,*
 612 2021a. URL <https://openreview.net/forum?id=VVdmjgu7pKM>.

613

614 Anirudh Goyal, Alex Lamb, Jordan Hoffmann, Shagun Sodhani, Sergey Levine, Yoshua Bengio, and
 615 Bernhard Schölkopf. Recurrent independent mechanisms. In *9th International Conference on
 616 Learning Representations, ICLR 2021, Virtual Event, Austria, May 3-7, 2021*. OpenReview.net,
 617 2021b. URL <https://openreview.net/forum?id=mLcmd1EUxy->.

618

619 Christian Gumbsch, Martin V Butz, and Georg Martius. Sparsely changing latent states for prediction
 620 and planning in partially observable domains. *Advances in Neural Information Processing Systems*,
 621 34:17518–17531, 2021.

622

623 Nan Rosemary Ke, Aniket Didolkar, Sarthak Mittal, Anirudh Goyal, Guillaume Lajoie, Stefan Bauer,
 624 Danilo Jimenez Rezende, Michael Mozer, Yoshua Bengio, and Chris Pal. Systematic evaluation of
 625 causal discovery in visual model based reinforcement learning. In Joaquin Vanschoren and Sai-Kit
 626 Yeung (eds.), *Proceedings of the Neural Information Processing Systems Track on Datasets and
 627 Benchmarks 1, NeurIPS Datasets and Benchmarks 2021, December 2021, virtual*, 2021. URL
 628 <https://datasets-benchmarks-proceedings.neurips.cc/paper/2021/hash/8f121ce07d74717e0bf21d122e04521-Abstract-round2.html>.

629

630 Thomas N. Kipf and Max Welling. Semi-supervised classification with graph convolutional networks.
 631 In *International Conference on Learning Representations*, 2017. URL <https://openreview.net/forum?id=SJU4ayYgl>.

632

633 Thomas N. Kipf, Elise van der Pol, and Max Welling. Contrastive learning of structured world models.
 634 In *8th International Conference on Learning Representations, ICLR 2020, Addis Ababa, Ethiopia,
 635 April 26-30, 2020*. OpenReview.net, 2020. URL <https://openreview.net/forum?id=H1gax6VtDB>.

636

637 Richard D. Lange and Konrad P. Kording. Causality in the human niche: lessons for machine
 638 learning. *CoRR*, abs/2506.13803, 2025. doi: 10.48550/ARXIV.2506.13803. URL <https://doi.org/10.48550/arXiv.2506.13803>.

639

640 Anson Lei, Bernhard Schölkopf, and Ingmar Posner. Spartan: A sparse transformer learning local
 641 causation. *arXiv preprint arXiv:2411.06890*, 2024.

642

643 Valentyn Melnychuk, Dennis Frauen, and Stefan Feuerriegel. Causal transformer for estimating
 644 counterfactual outcomes. In Kamalika Chaudhuri, Stefanie Jegelka, Le Song, Csaba Szepesvári,
 645 Gang Niu, and Sivan Sabato (eds.), *International Conference on Machine Learning, ICML 2022,*
 646 *17-23 July 2022, Baltimore, Maryland, USA*, volume 162 of *Proceedings of Machine Learning
 647 Research*, pp. 15293–15329. PMLR, 2022. URL <https://proceedings.mlr.press/v162/melnychuk22a.html>.

648 Andrew Y. Ng and Stuart Russell. Algorithms for inverse reinforcement learning. In Pat Langley
 649 (ed.), *Proceedings of the Seventeenth International Conference on Machine Learning (ICML 2000),*
 650 *Stanford University, Stanford, CA, USA, June 29 - July 2, 2000*, pp. 663–670. Morgan Kaufmann,
 651 2000.

652 Eshaan Nichani, Alex Damian, and Jason D. Lee. How transformers learn causal structure with
 653 gradient descent. In *Forty-first International Conference on Machine Learning, ICML 2024,*
 654 *Vienna, Austria, July 21-27, 2024*. OpenReview.net, 2024. URL [https://openreview.net/](https://openreview.net/forum?id=jNM4imlHZv)
 655 [forum?id=jNM4imlHZv](https://openreview.net/forum?id=jNM4imlHZv).

656 Judea Pearl. *Causality: Models, Reasoning and Inference*. Cambridge University Press, USA, 2nd
 657 edition, 2009. ISBN 052189560X.

658 Silviu Pitis, Elliot Creager, and Animesh Garg. Counterfactual data augmentation using locally
 659 factored dynamics. *Advances in Neural Information Processing Systems*, 33:3976–3990, 2020.

660 James Robins and Miguel Hernan. *Estimation of the causal effects of time-varying exposure*, pp.
 661 553–599. 08 2008. ISBN 978-1-58488-658-7. doi: 10.1201/9781420011579.ch23.

662 Raanan Y. Rohekar, Yaniv Gurwicz, and Shami Nisimov. Causal interpretation of self-
 663 attention in pre-trained transformers. In Alice Oh, Tristan Naumann, Amir Globerson,
 664 Kate Saenko, Moritz Hardt, and Sergey Levine (eds.), *Advances in Neural Information
 665 Processing Systems 36: Annual Conference on Neural Information Processing Systems 2023, NeurIPS
 666 2023, New Orleans, LA, USA, December 10 - 16, 2023*. URL http://papers.nips.cc/paper_files/paper/2023/hash/642a321fba8a0f03765318e629cb93ea-Abstract-Conference.html.

667 Paul K. Rubenstein, Stephan Bongers, Joris M. Mooij, and Bernhard Scholkopf. From deterministic
 668 odes to dynamic structural causal models. In *Conference on Uncertainty in Artificial Intelligence*,
 669 2016. URL <https://api.semanticscholar.org/CorpusID:2303037>.

670 Donald B. Rubin. Bayesian Inference for Causal Effects: The Role of Randomization. *The Annals of
 671 Statistics*, 6(1):34 – 58, 1978. doi: 10.1214/aos/1176344064. URL <https://doi.org/10.1214/aos/1176344064>.

672 Bertrand Russell. *Human Knowledge: Its Scope and Limits*. Routledge, London and New York,
 673 1948.

674 Wesley C. Salmon. *Scientific Explanation and the Causal Structure of the World*. Princeton University
 675 Press, 1984.

676 Franco Scarselli, Marco Gori, Ah Chung Tsoi, Markus Hagenbuchner, and Gabriele Monfardini. The
 677 graph neural network model. *IEEE Trans. Neural Networks*, 20(1):61–80, 2009. doi: 10.1109/
 678 TNN.2008.2005605. URL <https://doi.org/10.1109/TNN.2008.2005605>.

679 Bernhard Schölkopf, Francesco Locatello, Stefan Bauer, Nan Rosemary Ke, Nal Kalchbrenner,
 680 Anirudh Goyal, and Yoshua Bengio. Toward causal representation learning. *Proceedings of the
 681 IEEE*, 109(5):612–634, 2021.

682 Maximilian Seitzer, Bernhard Schölkopf, and Georg Martius. Causal influence detection for improv-
 683 ing efficiency in reinforcement learning. *Advances in Neural Information Processing Systems*, 34:
 684 22905–22918, 2021.

685 Xiao Shou, Debarun Bhattacharjya, Tian Gao, Dharmashankar Subramanian, Oktie Hassanzadeh,
 686 and Kristin P. Bennett. Pairwise causality guided transformers for event sequences. In Alice Oh,
 687 Tristan Naumann, Amir Globerson, Kate Saenko, Moritz Hardt, and Sergey Levine (eds.),
 688 *Advances in Neural Information Processing Systems 36: Annual Conference on Neural
 689 Information Processing Systems 2023, NeurIPS 2023, New Orleans, LA, USA, December 10 -
 690 16, 2023*. URL http://papers.nips.cc/paper_files/paper/2023/hash/91b047c5f5bd41ef56bfaf4ad0bd19e3-Abstract-Conference.html.

691 Brian Skyrms. Causal necessity. *Philosophy of Science*, 48(2):329–335, 1981. doi: 10.1086/289003.

702 Jake Topping, Francesco Di Giovanni, Benjamin Paul Chamberlain, Xiaowen Dong, and Michael M.
 703 Bronstein. Understanding over-squashing and bottlenecks on graphs via curvature. In *The Tenth In-*
 704 *ternational Conference on Learning Representations, ICLR 2022, Virtual Event, April 25-29, 2022.*
 705 OpenReview.net, 2022. URL <https://openreview.net/forum?id=7UmjRGzp-A>.
 706

707 Núria Armengol Urpí, Marco Bagatella, Marin Vlastelica, and Georg Martius. Causal action influence
 708 aware counterfactual data augmentation. *arXiv preprint arXiv:2405.18917*, 2024.
 709

710 Ashish Vaswani, Noam Shazeer, Niki Parmar, Jakob Uszkoreit, Llion Jones, Aidan N. Gomez,
 711 Lukasz Kaiser, and Illia Polosukhin. Attention is all you need. In Isabelle Guyon, Ulrike von
 712 Luxburg, Samy Bengio, Hanna M. Wallach, Rob Fergus, S. V. N. Vishwanathan, and Roman
 713 Garnett (eds.), *Advances in Neural Information Processing Systems 30: Annual Conference on*
 714 *Neural Information Processing Systems 2017, December 4-9, 2017, Long Beach, CA, USA*, pp.
 715 5998–6008, 2017. URL <https://proceedings.neurips.cc/paper/2017/hash/3f5ee243547dee91fdb053c1c4a845aa-Abstract.html>.
 716

717 Petar Veličković, Guillem Cucurull, Arantxa Casanova, Adriana Romero, Pietro Liò, and Yoshua
 718 Bengio. Graph attention networks. In *International Conference on Learning Representations*,
 719 2018. URL <https://openreview.net/forum?id=rJXMpikCZ>.
 720

721 Zizhao Wang, Xuesu Xiao, Zifan Xu, Yuke Zhu, and Peter Stone. Causal dynamics learning for
 722 task-independent state abstraction. *CoRR*, abs/2206.13452, 2022. URL <https://doi.org/10.48550/arXiv.2206.13452>.
 723

724 Christopher J. C. H. Watkins and Peter Dayan. Technical note q-learning. *Mach. Learn.*, 8:279–292,
 725 1992. doi: 10.1007/BF00992698. URL <https://doi.org/10.1007/BF00992698>.
 726

727 Marcel Weber. On the incompatibility of dynamical biological mechanisms and causal graphs.
 728 *Philosophy of Science*, 83(5):959–971, 2016. ISSN 00318248, 1539767X. URL <https://www.jstor.org/stable/26551794>.
 729

730 Moritz Willig, Tim Nelson Tobiasch, Florian Peter Busch, Jonas Seng, Devendra Singh Dhami,
 731 and Kristian Kersting. Systems with switching causal relations: A meta-causal perspective. In
 732 *The Thirteenth International Conference on Learning Representations, ICLR 2025, Singapore,*
 733 *April 24-28, 2025*. OpenReview.net, 2025. URL <https://openreview.net/forum?id=J9VogDTa1W>.
 734

735 Kevin Xia, Kai-Zhan Lee, Yoshua Bengio, and Elias Bareinboim. The causal-neural con-
 736 nection: Expressiveness, learnability, and inference. In Marc'Aurelio Ranzato, Alina
 737 Beygelzimer, Yann N. Dauphin, Percy Liang, and Jennifer Wortman Vaughan (eds.), *Ad-*
 738 *vances in Neural Information Processing Systems 34: Annual Conference on Neural In-*
 739 *formation Processing Systems 2021, NeurIPS 2021, December 6-14, 2021, virtual*, pp.
 740 10823–10836, 2021. URL <https://proceedings.neurips.cc/paper/2021/hash/5989add1703e4b0480f75e2390739f34-Abstract.html>.
 741

742 Keyulu Xu, Weihua Hu, Jure Leskovec, and Stefanie Jegelka. How powerful are graph neural
 743 networks? In *International Conference on Learning Representations*, 2019. URL <https://openreview.net/forum?id=ryGs6iA5Km>.
 744

745 Mengyue Yang, Furui Liu, Zhitang Chen, Xinwei Shen, Jianye Hao, and Jun Wang. Causalvae:
 746 Disentangled representation learning via neural structural causal models. In *2021 IEEE/CVF*
 747 *Conference on Computer Vision and Pattern Recognition (CVPR)*, pp. 9588–9597, 2021. doi:
 748 10.1109/CVPR46437.2021.00947.
 749

750 Matej Zecevic, Devendra Singh Dhami, Petar Velickovic, and Kristian Kersting. Relating graph
 751 neural networks to structural causal models. *CoRR*, abs/2109.04173, 2021. URL <https://arxiv.org/abs/2109.04173>.
 752

753

756 A OBJECT-CENTRIC CAUSAL DYNAMICS
757758 Consider two objects O_1 and O_2 (depicted in magenta) with a force F (depicted in violet) acting on
759 them:
760

761
762 $O_1 \xrightarrow{F} O_2$
763

764 This recovers the familiar structure of a directed acyclic graphs (DAGs) from Pearl’s causal formalism
765 Pearl (2009). However, in physical interactions, such as in a collision, it is not always clear which
766 object is the “cause” since both are affected simultaneously. A more intuitive representation would
767 be a bidirectional edge:
768

769
770 $O_1 \xleftrightarrow{F} O_2$
771

772 However, DAGs prohibit cycles and bidirectional edges. To resolve this, we introduce *temporal*
773 *dynamics* which represent causal effects as unfolding over time rather than as a simultaneous influence.
774 Thus, a collision between object O_1 and object O_2 yields forces F_2 and F_3 as emerging from the past
775 state and influencing future object states:
776

777
$$\begin{array}{ccc} O_1^t & \xrightarrow{F_1} & O_1^{t+1} \\ & \searrow F_2 & \swarrow F_3 \\ O_2^t & \xrightarrow{F_4} & O_2^{t+1} \end{array}$$

778
779
780

781 Yet, this representation still has drawbacks. Specifically, we break the identity of the force F into F_2
782 and F_3 which, in principle, can act as separate causal links (F_1 and F_4 can be thought of as inertia).
783 This becomes apparent when interventions are applied. Let us imagine that somebody picks up object
784 O_1 just before it collides with O_2 . This can be represented by a do-calculus-like intervention applied
785 to either O_1^t or O_1^{t+1} :
786

787
$$\begin{array}{ccc} \cancel{\bullet} O_1^t & \xrightarrow{F_1} & O_1^{t+1} \\ & \searrow F_2 & \swarrow F_3 \\ O_2^t & \xrightarrow{F_4} & O_2^{t+1} \end{array} \qquad \begin{array}{ccc} O_1^t & \xrightarrow{F_2} & \cancel{\bullet} O_1^{t+1} \\ O_2^t & \xrightarrow{F_4} & O_2^{t+1} \end{array}$$

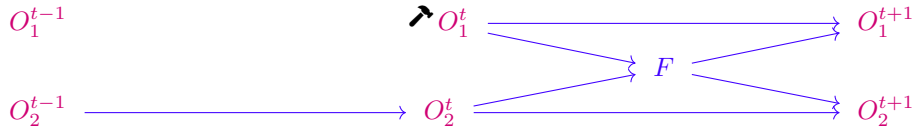
788
789
790

791 When the intervention is applied to O_1^t , the graph structure is preserved, thus implying a no-collision
792 scenario (one of the balls was lifted). Yet, the same graph can also imply a collision scenario. This
793 kind of setup necessitates having causal links between objects that can potentially collide irrespective
794 of the actualization of said collision. While this approach can work in principle, it results in extremely
795 dense graphs with complete subgraphs per time step, especially in cluttered scenes. Ideally, we would
796 like to have causal links in our graph if there is an actualized interaction between the involved objects.
797798 On the other hand, intervening on O_1^{t+1} results in a graph with counter-intuitive interpretation: O_1
799 gets lifted at time step $t + 1$, while O_2 behaves as if a collision has happened. This is due to the split
800 of F into F_2 and F_3 since an intervention removes F_3 while leaving F_2 untouched. To tackle the
801 aforementioned issues, let us re-imagine force edges as nodes and re-introduce F_2 and F_3 as a single
802 node F and extend the time horizon by a step.
803

804
$$\begin{array}{ccc} O_1^{t-1} & \longrightarrow & O_1^t & \xrightarrow{F} & O_1^{t+1} \\ O_2^{t-1} & \longrightarrow & O_2^t & \xrightarrow{F} & O_2^{t+1} \end{array}$$

805
806
807

808 Now, imagine, just like before, the ball O_1 gets picked up at time step t . In do-calculus terms, this
809 amounts to intervention to O_1^t which results in mutilation of the edge $O_1^{t-1} \rightarrow O_1^t$

810
811
812
813
814

815 While the problem of splitting of the force identity seems to be resolved here, the graph structure
 816 modeling the collision remains preserved despite the intervention. As mentioned before, this can
 817 be addressed by complete subgraphs per time step, which is not desirable for our purposes. This
 818 problem arises due to the inclusion of time dynamics into our graphs. Unlike in Pearlian Causality,
 819 in physics, interventions at a time step have implications for the causal connections corresponding
 820 to downstream time steps. To account for that, we have to re-imagine interventions under a new
 821 framework that takes physical processes and time into account (see Algorithm 1).

B MODEL DETAILS

B.1 INDUCTIVE BIAS

827 We introduce two inductive biases: (1) limiting each force node to interact with exactly two objects to
 828 reflect pairwise interactions, and (2) enforcing a bidirectional mirroring constraint to ensure temporal
 829 coherence in causal attribution. Formally the latter is defined as:

830
831
832
833
834
835

$$\begin{aligned} \forall i, j, k, t : \{E(O_i^t, F_j^{t+1}), E(O_k^t, F_j^{t+1})\} \subset C_E^t \implies \\ E(F_j^{t+1}, O_i^{t+1}) \in G_E^t \vee E(F_j^{t+1}, O_k^{t+1}) \in G_E^t, \\ \forall i, j, t : E(F_j^{t+1}, O_i^{t+1}) \in G_E^t \implies E(O_i^t, F_j^{t+1}) \in G_E^t. \end{aligned}$$

B.2 VECTOR CONSTRAINTS

837 *Causal* relevance is coded by C . Perturbing the sub-vectors of the parent with $C = 0$ does not affect
 838 the child nodes, i.e., only the causally-relevant $C = 1$ sub-vectors affect the child nodes:

840
841

$$\forall t, i : F_j^{t+1,1PM} = \tilde{F}_j^{t+1,1PM} \implies f_O(O_i^t, \{F_j^{t+1}\}_{j|(j,i) \in I^t}; \theta_O) = f_O(O_i^t, \{\tilde{F}_j^{t+1}\}_{j|(j,i) \in I^t}; \theta_O).$$

842 *Control* relevance is coded by P . Two force vectors whose sub-vectors with $P = 1$ are identical have
 843 identical control functions that are conditioned on them, i.e., control functions are conditioned only
 844 on the control-relevant sub-vectors :

845

846
847

$$\forall t : F_j^{t+1,C1M} = \tilde{F}_j^{t+1,C1M} \implies \rho_{O \leftrightarrow \tilde{F}}^t = \rho_{O \leftrightarrow \mathcal{F}}^t.$$

848 Lastly, *mutability* is coded by M . If $M = 0$, the corresponding sub-vector does not change over time,
 849 i.e., an immutable sub-vector does not change over time: $\forall t, j : F_j^{t,CP0} = \tilde{F}_j^{t+1,CP0}$.

850

B.3 CAUSAL PROCESS BLOCK

853
854

Given the data F^t, O_1^t, \dots, O_n^t , and the chosen indices J^t , we calculate F^{t+1} in the following way:

855
856

$$F^{t+1} := f_F(F^t, O_1^t, \dots, O_n^t, J^t \mid \theta_F),$$

857

with O^{t+1} also calculated similarly.

858
859
860

$$\text{gate} := \frac{1}{|J^t|} \sum_{i \in J^t} (O_i^{t,1PM} W_{\text{gate}}^F) W_{\text{output}}^F,$$

861

$$\text{residual} := \text{gate} + F^{t,CP1},$$

862
863

$$F^{t+1,CP1} := \chi_{\text{gate} \neq 0} \odot \text{FFN}(\text{Norm}(\text{residual})) + \text{residual},$$

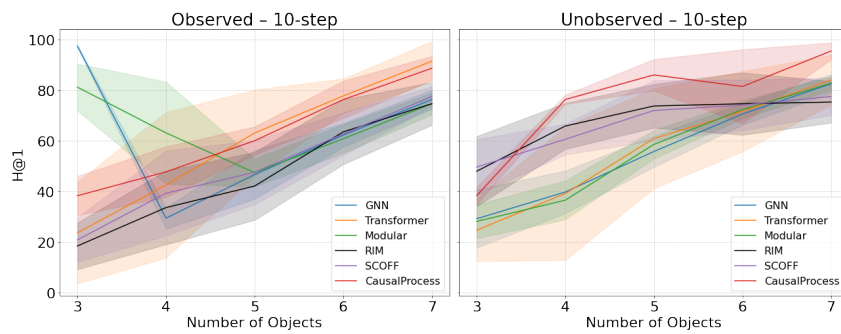
$$F^{t+1} := [F^{t+1,CP1}; F^{t,CP0}],$$

864 where $\theta_F := \{W_{\text{gate}}^F, W_{\text{output}}^F, W_1^F, W_2^F, b_1^F, b_2^F\}$ FFN is a feed-forward neural network $\text{FFN}(x) :=$
 865 $\max(0, xW_1^F + b_1^F) W_2^F + b_2^F$, W_{gate}^F is the analogue of the attention mechanisms value token
 866 projection, and W_{output}^F is again the analogous out-projection that maps the token from the attention
 867 dimension back to residual dimension (Vaswani et al., 2017)
 868

869
 870
 871
 872

873 C PLOTS

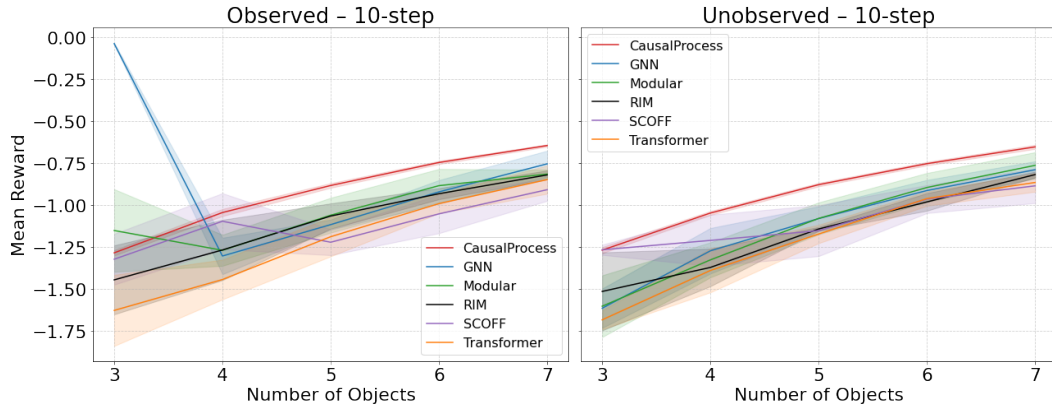
874
 875
 876
 877
 878
 879
 880



881
 882
 883
 884
 885
 886
 887
 888
 889
 890

893 Figure 7: Prediction metric vs number of objects for 10-steps.
 894

895
 896
 897
 898
 899
 900
 901
 902



914
 915
 916
 917

913 Figure 8: Downstream RL results over number of objec. Mean reward vs number of objects. All
 914 results are the average of 10 seeds

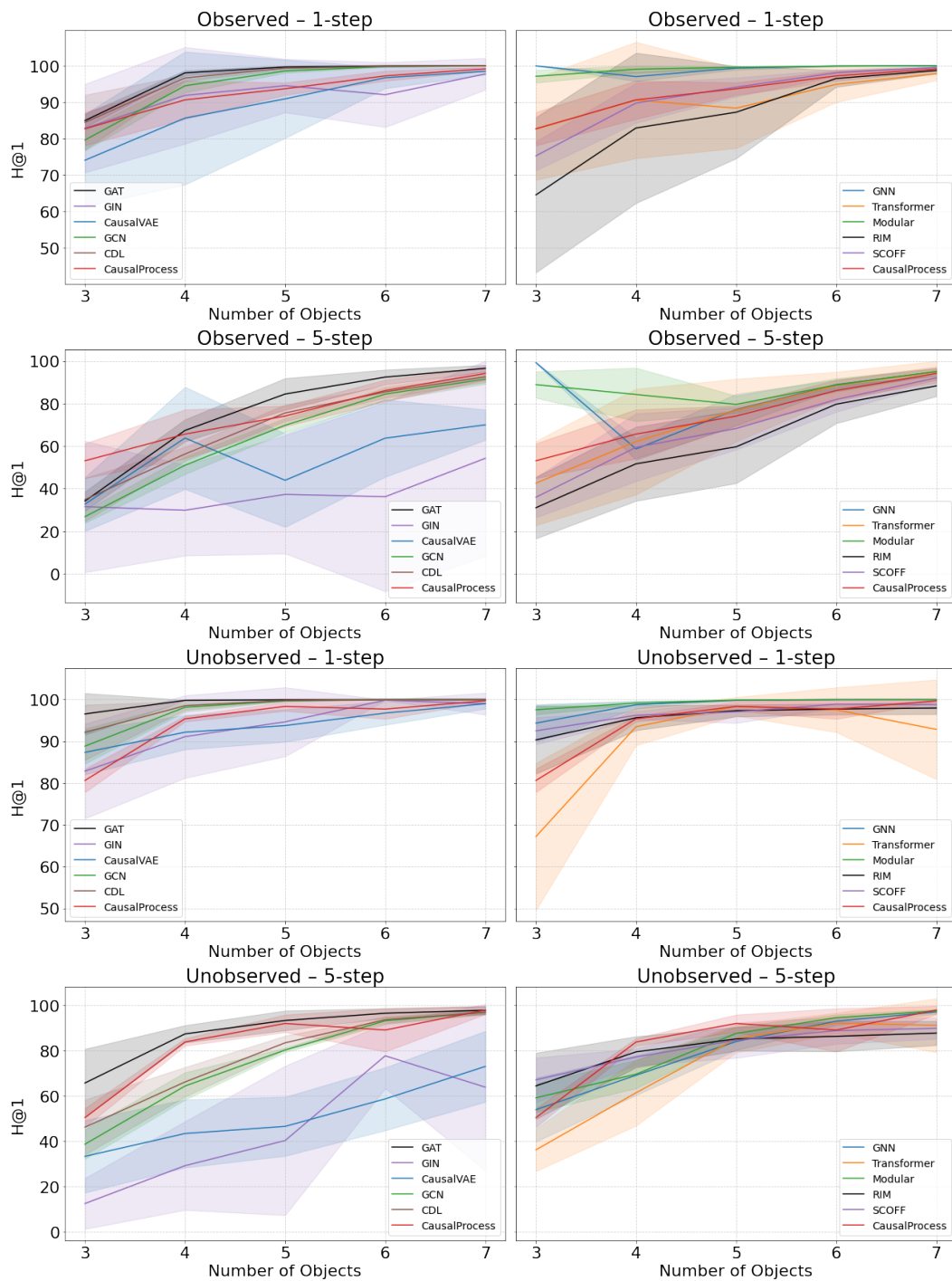


Figure 9: Prediction metric vs number of objects after 1 and 5 steps (average of 10 seeds).

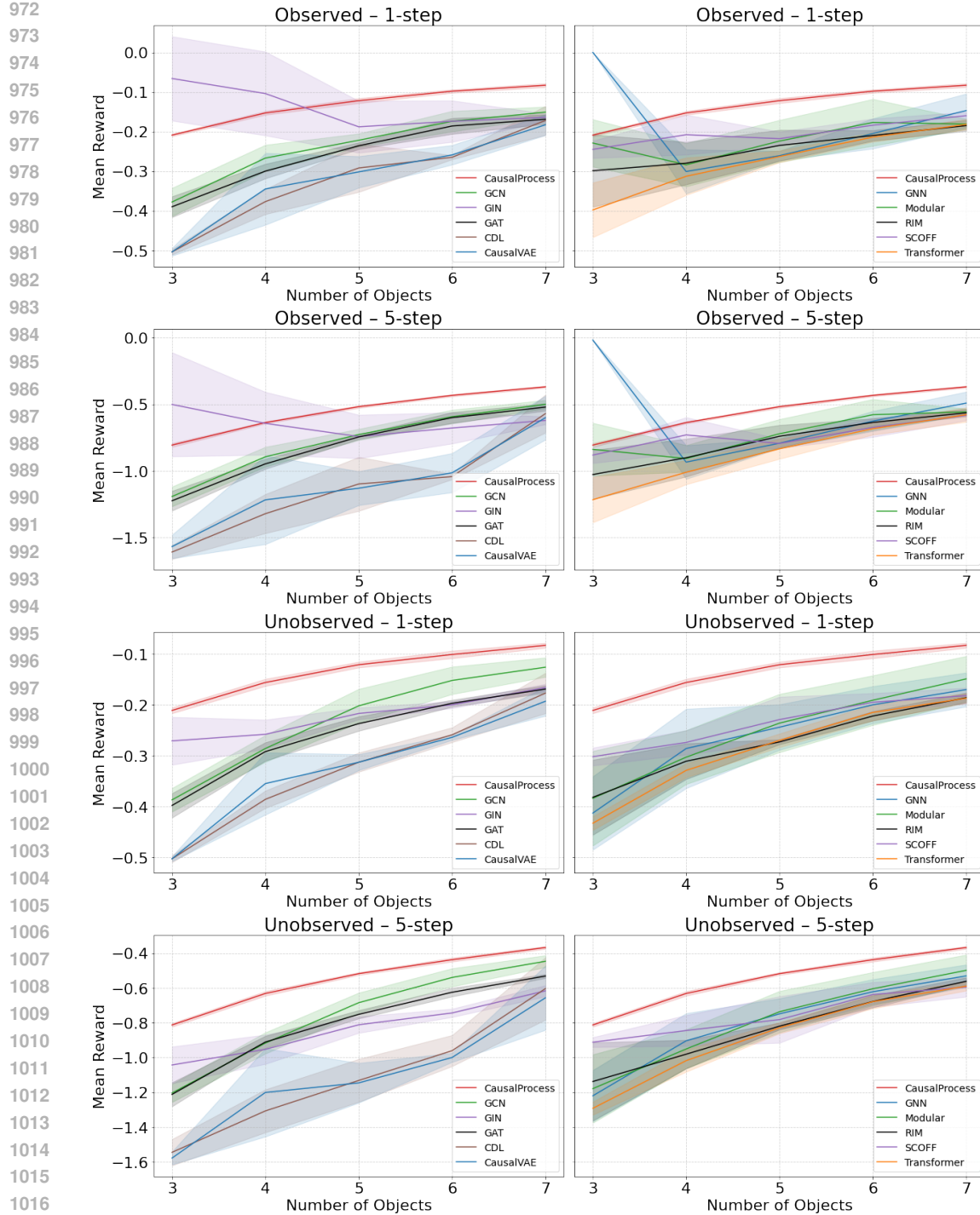


Figure 10: Mean reward vs number of objects after 1 and 5 steps (average of 10 seeds).

1026 **D ALGORITHMS**
10271028 **Algorithm 1** Interventions under Causal Process Framework

1029

1030 **Require:** $\mathcal{F}^t, \mathcal{O}^t, f_F, f_O, \rho_{\mathcal{O} \leftrightarrow \mathcal{F}}^t, \rho_{\mathcal{O}}^t, act\left(O_*^{\tilde{t}}\right), G_{\mathcal{O}^1: \mathcal{O}^T}, t \in \{1, \dots, T\}, i \in \{1, \dots, I\}, j \in \{1, \dots, J\}$

1031 **Ensure:** Output result $\tilde{G}_{\mathcal{O}^1: \mathcal{O}^T}$

1032 1: Initialize $\tilde{\mathcal{O}}^{\tilde{t}-1} := \left\{O_*^{\tilde{t}-1}\right\} \dot{\cup} \mathcal{O}^{\tilde{t}-1}$

1033 2: Initialize $\tilde{\mathcal{F}}^{\tilde{t}} := \mathcal{F}^{\tilde{t}}$

1034 3: Initialize $J^t := \{(i, j)\}$ s.t. $E\left(O_i^{\tilde{t}-1}, F_j^{\tilde{t}}\right) \in G_{\mathcal{O}^{\tilde{t}-1}: \mathcal{F}^{\tilde{t}}}^{\mathcal{E}}$

1035 4: Initialize $\tilde{G}_{\mathcal{O}^1: \mathcal{O}^{\tilde{t}-1}} := G_{\mathcal{O}^1: \mathcal{O}^{\tilde{t}-1}}$

1036 5: **for** $t = \tilde{t}, \dots, T$ **do** ▷ Loop from $t = \tilde{t}$ up to T

1037 6: $\tilde{G}_{\mathcal{O}^1: \mathcal{F}^t} := \left(\tilde{\mathcal{F}}^t \dot{\cup} \tilde{G}_{\mathcal{O}^1: \mathcal{O}^{t-1}}^{\mathcal{V}}, \left\{E\left(\tilde{O}_i^{t-1}, \tilde{F}_j^t\right)\right\}_{(i, j) \in J^t} \dot{\cup} \tilde{G}_{\mathcal{O}^1: \mathcal{O}^{t-1}}^{\mathcal{E}}\right)$ ▷ Update the graph

1038 7: $I^t \sim \rho_{\tilde{\mathcal{O}} \leftrightarrow \tilde{\mathcal{F}}}^t$ ▷ Sample new edges

1039 8: **for** $i = 1, \dots, I$ **do** ▷ Loop from $i = 1$ up to I

1040 9: $\tilde{O}_i^t := f_O\left(\tilde{O}_i^{t-1}, \left\{\tilde{F}_j^t\right\}_{j|(j, i) \in I^t}\right)$ ▷ Update the nodes

1041 10: **end for**

1042 11: $\tilde{G}_{\mathcal{O}^1: \mathcal{O}^t} := \left(\tilde{\mathcal{O}}^t \dot{\cup} \tilde{G}_{\mathcal{O}^1: \mathcal{F}^t}^{\mathcal{V}}, \left\{E\left(\tilde{F}_j^t, \tilde{O}_i^t\right)\right\}_{(j, i) \in I^t} \dot{\cup} \tilde{G}_{\mathcal{O}^1: \mathcal{F}^t}^{\mathcal{E}}\right)$ ▷ Update the graph

1043 12: $J^t \sim \rho_{\tilde{\mathcal{O}}}^t$ ▷ Sample new edges

1044 13: **for** $j = 1, \dots, J$ **do** ▷ Loop from $j = 1$ up to J

1045 14: $\tilde{F}_j^{t+1} := f_F\left(\tilde{F}_j^t, \left\{\tilde{O}_i^t\right\}_{i|(i, j) \in J^t}\right)$ ▷ Update the nodes

1046 15: **end for**

1047 16: **end for**

1048 17: **return** $\tilde{G}_{\mathcal{O}^1: \mathcal{O}^T}$

1049

1050

1051

1052

1053

1054

1055

1056

1057

1058

1059

1060

1061

1062

1063

1064

1065

1066

1067

1068

1069

1070

1071

1072

1073

1074

1075

1076

1077

1078

1079